PAPER

Morphologically tuned CuO–ZnO–CeO$_2$ catalyst for CO$_2$ hydrogenation to methanol

Suresh Kanuri,[a] Satyapaul A. Singh, [ID] [a] Appala Naidu Uttaravalli,[b] Sounak Roy [ID] [c] and Srikanta Dinda [ID] *[a]

Morphologically modified composite CuO–ZnO–CeO$_2$ catalysts were synthesized using a single-step hydrothermal technique. The study highlights the influence of solvent on the structural and physico-chemical properties of the catalysts. Various techniques, such as XRD, FE-SEM, BET, XPS, and H$_2$-TPR, were used to analyze the catalyst properties. Among the synthesized materials, the catalyst, prepared with a *N,N*-dimethyl formamide (DMF)-to-metal nitrates ratio of 20 (named as CZC-1), showed enhanced active sites in the form of surface features such as nanowire-like morphology, large surface area, low crystallite size, increased oxygen vacancies, and high CuO dispersion. A bench-scale fixed-bed flow reactor was used to examine the catalytic performance of the catalysts. At 225 °C reactor temperature, 30 bar reactor pressure, and with a space velocity of 6000 cm^3 g$_{cat}^{-1}$ h^{-1}, the CZC-1 catalyst showed 13.6% CO$_2$ conversion and 74.1% methanol selectivity. *In situ* diffuse reflectance infrared Fourier transform spectroscopy (DRIFTS) analysis confirmed the carbonate–formate–methoxy reaction pathway for methanol formation using the CZC-1 catalyst.

1. Introduction

The concentration of CO$_2$ in the atmosphere is increasing rapidly due to swift industrialization and fossil fuel consumption. According to National Oceanic & Atmospheric Administration (NOAA) research, the average concentration of CO$_2$ in the atmosphere is about 422 ppm, which has increased by 6.1% during the last decade. An effective way to minimize CO$_2$ emissions is the direct hydrogenation of CO$_2$ using renewable hydrogen.[1] It is also an attractive option for the generation of renewable energy chemicals and fuels such as dimethyl ether (DME), formic acid, dimethyl carbonate (DMC), methane, and methanol (MeOH).[2] Among CO$_2$-hydrogenated products, methanol (MeOH) has an advantage due to its versatile applications including a clean fuel or gasoline additive to reduce greenhouse gas emissions.[3] Also, MeOH is in great demand to produce industrial chemicals such as olefins, formaldehyde, acetic acid, methyl *tert*-butyl ether, and dimethyl ether.[4,5] Numerous investigations have been carried out on the catalytic hydrogenation of CO$_2$ to MeOH. Two major reactions, CO$_2$ + 3H$_2$ ↔ CH$_3$OH + H$_2$O and CO$_2$ + H$_2$ ↔ CO + H$_2$O, can occur

simultaneously during the synthesis of MeOH from the hydrogenation of pure CO$_2$.[6] The two major challenges involved in the direct hydrogenation of CO$_2$ to MeOH are poor reactivity of CO$_2$ towards MeOH formation and CO formation.[7] Thus, the process of converting gaseous CO$_2$ into MeOH requires an appropriate catalyst. Traditionally, syngas (a mixture of CO, CO$_2$, and H$_2$) has been used to produce MeOH in the presence of CuO–ZnO/Al$_2$O$_3$ catalyst.[8]

In recent studies, CeO$_2$-assisted transition metal-based catalysts have been examined for the synthesis of MeOH from CO$_2$ and H$_2$. A CeO$_2$-supported CuO/CeO$_2$ nanorod-shaped catalyst showed about 2% CO$_2$ conversion and 88% MeOH selectivity under 240 °C and 20 bar pressure.[9] Tan *et al.* prepared CeO$_2$ nanotubes using precipitation followed by a hydrothermal method and doped CuO and NiO into the CeO$_2$ support by an impregnation technique.[10] At 260 °C and 30 bar, the CuNi$_2$/CeO$_2$ catalyst showed 17.8% CO$_2$ conversion and 78.8% MeOH selectivity. Cu/CeO$_2$ and Cu/ZnO/CeO$_2$ catalysts were synthesized using flame spray pyrolysis technique and a 40 wt% CuO containing ZnO–CeO$_2$ catalyst demonstrated 5% CO$_2$ conversion and 50% MeOH selectivity at 250 °C and 30 bar pressure.[11] A 5 wt% Cu on CeO$_2$, and 1 wt% In and 5 wt% Cu on CeO$_2$ catalysts were synthesized using a two-step (hydrothermal followed by solvent-free) synthesis method.[12] The In-incorporated Cu/CeO$_2$ catalyst revealed improved Cu surface area and Cu dispersion, and the catalyst showed 7.6% CO$_2$ conversion and 95% MeOH selectivity at 200 °C and 30 bar pressure. Using a co-precipitation technique, Singh *et al.* synthesized CuO/ZnO, CuO/ZrO$_2$, and CuO/CeO$_2$ catalysts with

[a]Department of Chemical Engineering, Birla Institute of Technology and Science (BITS) Pilani, Hyderabad Campus, Hyderabad, Telangana-500078, India. E-mail: srikantadinda@hyderabad.bits-pilani.ac.in; Fax: +91-4066303998; Tel: +91-4066303586

[b]Department of Chemical Engineering, B. V. Raju Institute of Technology, Narsapur, Medak Dist., 502313, Telangana, India

[c]Department of Chemistry, Birla Institute of Technology and Science (BITS) Pilani, Hyderabad Campus, Hyderabad, Telangana-500078, India

40 wt% CuO loading in each case.[13] Because of higher oxygen vacancies and basic site densities, the CuO/CeO$_2$ catalyst demonstrated higher MeOH selectivity (~91%) at 220 °C and 30 bar compared to the CuO/ZnO and CuO/ZrO$_2$ catalysts. Zaman *et al.* synthesized Ca–PdZn/CeO$_2$ catalyst using sol–gel technique and examined the influence of Ca loadings on MeOH selectivity.[14] The 5 wt% Ca loaded PdZn/CeO$_2$ catalyst showed 16% CO$_2$ conversion and 93% MeOH selectivity at 230 °C and 20 bar. The interactions between CuO and CeO$_2$ nanorods were examined and correlated with active site concentration of Cu$^+$ species and oxygen vacancies.[15] The tungsten-doped Cu/CeO$_2$ catalyst showed a 10-fold more MeOH space-time yield (STY$_{MeOH}$) than the Cu/CeO$_2$ catalyst at 250 °C and 35 bar.[16] A 5 mol% In loaded Cu/CeO$_2$ catalyst exhibits 99.3% MeOH selectivity at 200 °C and 30 bar.[17] Khobragade *et al.* studied the influence of CeO$_2$ morphology (polyhedral, rod, cube, and polygonal) on methanol yield.[18] At 260 °C and 50 bar, the polyhedral-shaped CeO$_2$-supported Pd catalyst demonstrated 1290 g$_{MeOH}$ kg$_{cat}$$^{-1}$ h^{-1} of STY$_{MeOH}$.

From the literature study, the physico-chemical properties of the catalysts, such as Cu dispersion, Cu surface area, metal–support interactions, and oxygen vacancies, were found to be the crucial parameters in composite catalysts for MeOH synthesis from CO$_2$ hydrogenation.[18] Interestingly, the CeO$_2$ morphology significantly improved the above-mentioned properties of the composite catalyst.[19,20] However, the one-step synthesis of morphologically tuned CeO$_2$-supported catalysts is still intriguing. In this work, a single-step hydrothermal technique was used to synthesize morphologically tuned composite CuO–ZnO–CeO$_2$ catalysts. To elucidate the relationship between catalyst surface properties and activity for MeOH synthesis from CO$_2$ hydrogenation reaction, standard characterization techniques such as X-ray diffraction (XRD), Brunauer–Emmett–Teller (BET), scanning electron microscopy (SEM), X-ray photoelectron spectroscopy (XPS), temperature programmed reduction (H$_2$-TPR), and *in situ* diffuse reflectance infrared Fourier transform spectroscopy (DRIFTS), were used. Further, the performance of the CeO$_2$-supported catalysts toward methanol synthesis was investigated in a high-pressure fixed-bed flow reactor. The main aim of the current study is to investigate the structure–property–performance relationship of a catalyst towards the desired product yield.

2. Materials and methods

2.1. Materials used

Cupric nitrate trihydrate (Cu(NO$_3$)$_2$·3H$_2$O, 99.5%), zinc nitrate hexahydrate (Zn(NO$_3$)$_2$·6H$_2$O, 99%), ammonium ceric nitrate ((NH$_4$)$_2$Ce(NO$_3$)$_6$, 99%), *N,N*-dimethyl formamide (DMF) (C$_3$H$_7$NO, 99%), dimethyl ether (99.9%) and methanol (99.9%), were procured from Sisco Research Laboratories Pvt. Ltd., India, and were used without additional purification. For the CO$_2$ hydrogenation experiments, CO$_2$ (99.9%) and H$_2$ (99.9%) gases were acquired from Chemix Specialty Gases and Equipment, India. A gas mixture consisting of 10.9% H$_2$, 8.2% CH$_4$, 5.2% CO, 15% CO$_2$, and balanced N$_2$ was procured from Chemix

Specialty Gases and Equipment, India, for the calibration of gas chromatography.

2.2. Catalyst preparation

A hydrothermal technique was employed to synthesize a series of CuO–ZnO–CeO$_2$ (CZC) catalysts using a Teflon-lined high-pressure autoclave fitted with a stirrer and temperature controller. Three catalysts (namely, CZC-1, CZC-2, and CZC-3) were prepared for a fixed composition of 20 wt% CuO, 20 wt% ZnO, and 60 wt% CeO$_2$, but with different synthesis protocols. In a typical synthesis (*e.g.*, for 10 g of CZC-1 catalyst), 6.1 g of Cu(NO$_3$)$_2$·3H$_2$O, 7.3 g of Zn(NO$_3$)$_2$·6H$_2$O, and 19.1 g of (NH$_4$)$_2$Ce(NO$_3$)$_6$ were dissolved in 130 mL of DMF in a conical flask. The mixture was stirred for 5 h under a stirring speed of 300 rpm. Then the solution was transferred into a 300 mL capacity autoclave and heated at 150 °C for 9 h, and then cooled to room temperature through natural convection. The resultant slurry was filtered and washed with deionized water several times. Then the obtained filter cake was dried at 100 °C for 12 h in a hot-air oven. The dried mass was crushed into powder form and calcined at 500 °C for 6 h in a muffle furnace. A similar process was used for the synthesis of the CZC-2 catalyst but with a different value of DMF-to-metal nitrates mole ratio. The DMF-to-metal nitrates (Cu^{2+} + Zn^{2+} + Ce^{3+}) mole ratio used for the CZC-1 and CZC-2 catalysts were 20 and 30, respectively. For the synthesis of the CZC-3 catalyst, during the hydrothermal process, the nitrates and DMF mixture was stirred at a speed of 300 rpm in addition to the procedure followed for the CZC-1 during its preparation.

2.3. Catalyst characterization

A powder X-ray diffraction instrument (Ultima-IV, Rigaku) with a Cu-Kα radiation source was employed to investigate the crystalline properties of the catalysts. A scan rate of 5° min^{-1} and a step size of 0.01° were used to measure the diffraction pattern throughout the 2θ range of 10° to 90°. The total surface area and pore volume of the CeO$_2$-supported catalysts were calculated from N$_2$-adsorption isotherms at −196 °C using a BELSORP-mini II instrument. Prior to the adsorption analysis, the catalysts were degassed for two hours at 200 °C under vacuum. An Everhart–Thornley detector paired with a field-emission scanning electron microscope (Apreo LoVac, FEI) was used to identify the surface morphology of the catalysts under vacuum with the accelerating voltage set to 20 kV. The samples were sputtered with gold before analysis to increase their electrical conductivity and produce high-quality micrographs. The oxidation states of the elements present in the catalyst samples were determined using an X-ray photoelectron spectroscope (K-Alpha, Thermo Fisher). An Al Kα emissive source with an energy range of 0–1200 eV and a step length of 1 eV was used to scan the catalyst specimen. The Cu 2p, Zn 2p, Ce 3d, and O 1s orbitals electronic characteristics were examined, and each XPS spectra was calibrated using graphitic carbon with a binding energy of 284.8 eV. A TPD equipment (Mayura Analytical LLP) paired with a thermal conductivity detector (TCD) was used to conduct the H$_2$-TPR study. The TPR experiments were

performed in a quartz tube reactor with 30 ± 2 mg of catalyst sample. At a flow rate of 50 mL min^{-1}, a gas mixture consisting of 5 vol% H$_2$ and 95 vol% N$_2$ was passed continuously through the catalyst bed. Using a PID temperature controller, the reactor was heated from ambient temperature (≈ 25 °C) to 800 °C at a heating rate of 10 °C min^{-1}. Fourier Transform Infrared Spectroscopy (FTIR) instrument (Alpha-II, Bruker) coupled with silicon carbide rod, as IR source, and deuterated triglycine sulphate detector was used to examine the presence of functional groups in liquid products. The diamond crystal used for holding the test sample was cleaned thoroughly with isopropyl alcohol to eradicate any potential surface contaminants. A wavenumber spanning from 500 cm^{-1} to 4000 cm^{-1} was used to record the IR spectra with 16 scans and a resolution of 4 cm^{-1}. Before analyzing test samples, a background spectrum was recorded without a test sample. Then, one drop of the test sample was placed on the diamond crystal and gathered the infrared spectrum of the test samples. The *in situ* diffuse reflectance infrared Fourier transform spectroscopy (DRIFTS) experiments were conducted using a zinc selenide window diffuse reflectance cell (Harrick Praying Mantis) coupled with an FTIR spectrometer (Spectrum 3, PerkinElmer). A time-based kinetic mode for a duration of 60 minutes was used to acquire the IR spectra. To remove surface-adsorbed species or impurities, the catalyst sample was heated in the sample holder for 1 h at 200 °C under a N$_2$ flow rate of 100 mL min^{-1}. Subsequently, the background spectrum was collected under these circumstances. Switched the 25 mL min^{-1} of CO$_2$ and 75 mL min^{-1} of H$_2$ flows, stopped the N$_2$ flow, and run the time-based kinetic mode to collect the IR spectra.

2.4. CO$_2$ hydrogenation experiment

The catalytic activity of the CuO–ZnO–CeO$_2$ catalysts was tested in a bench-scale fixed-bed flow reactor (length = 300 mm, and inner diameter = 10 mm) packed with 3.0 ± 0.1 g of catalyst. The schematic of the experimental setup is shown in Fig. 1. A total flow of 300 cm^3 min^{-1} of feed gas comprising 25% CO$_2$ and 75% H$_2$ was regulated to maintain an H$_2$/CO$_2$ mole ratio of 3. A back-pressure regulator was used to adjust the reactor pressure to the required level. The K-type thermocouple was used to monitor the catalyst bed temperature. Each experiment was performed for approximately two hours to collect a sufficient amount of the liquid product. A multichannel gas chromatography (Agilent 490 Micro GC) instrument was used to find the composition of the product gas. The liquid product was analyzed using gas chromatography equipment (Agilent 7820A) coupled with a Zebron (ZB-WAXplus) capillary column.

3. Results and discussion

3.1. XRD analysis

The X-ray diffraction patterns of the calcined CZC catalysts are shown in Fig. 2. In all the diffraction patterns, the peaks at 2θ values of 29.7°, 33.2°, 49.9°, and 69.0° correspond to the cubic structure of CeO$_2$ lattice planes of (1 1 1), (2 0 0), (2 2 0), and (4 0 0) (ref. JCPDS 001-0800). The diffraction peaks at 2θ values of 34.2° (2 0 0), 36.6° (1 0 1), and 57.5° (1 1 0) indicate the hexagonal ZnO phase (ref. JCPDS 075-1526). The peaks attributed to the 2θ values of 35.5° (0 0 2), 39.8° (1 1 1), 48.7° (−2 0 2), and 67.5° (1 1 3) signify the presence of the monoclinic phase of CuO (ref. JCPDS 074-1040). The broadening of the diffraction peaks in the XRD patterns indicates that the CeO$_2$-supported catalysts are likely nanocrystalline. The average crystallite size of the CZC catalysts was determined by Scherrer's equation (eqn (1)) and the estimated values are presented in Table 1. The average crystallite size of CZC catalysts grows from 9.1 nm to 12.1 nm as the DMF-to-metal nitrates mole ratio increases from 20 to 30. The crystallite size is further increased to 17.8 nm when the catalyst is synthesized under stirring and a DMF-to-metal nitrates mole ratio of 20. From the analysis, it is observed that, during the catalyst synthesis, stirring and the DMF-to-metal nitrates mole ratio have a direct relationship to the catalyst crystallite size.

$$D = \frac{k\lambda}{\beta \cos \theta} \qquad (1)$$

where, D is crystallite size, k is Scherrer's constant (0.94), λ is X-ray wavelength (1.54 Å), β is full-width half-maximum of diffraction peak, θ is half of the diffraction angle (2θ).

3.2. Surface area and pore size analysis

Fig. 3 shows the N$_2$ adsorption–desorption isotherms of CZC catalysts. The catalysts exhibit a typical shape of type-IV adsorption isotherms with a hysteresis loop. The existence of a hysteresis loop indicates the presence of mesopores in the CZC catalysts. Table 1 displays the total pore volume and BET surface area of the CZC-1, CZC-2, and CZC-3 catalysts. The total surface area and pore volumes of the CZC catalysts declined from 51.1 m^2 g^{-1} to 36.6 m^2 g^{-1} when the DMF-to-metal nitrates mole ratio increased from 20 to 30. The surface area further decreased to 14.1 m^2 g^{-1} when the catalyst was synthesized under stirring. The apparent reduction in surface area might be attributed to the increased DMF concentration and the presence of stirring, which accelerates the rate of nucleation and growth of catalyst particles. The findings obtained from the BET and XRD analysis were directly correlated with one another.

3.3. SEM analysis

The SEM micrographs of the calcined CZC catalysts exhibit morphological variations, as shown in Fig. 4. As the DMF-to-metal nitrates mole ratio varies from 20 to 30, three distinct morphologies, such as nanowire, nanorod, and nanoleaf, are observed. Coconut shell morphology was obtained for the catalyst prepared under stirring. Initially, nanoparticles might be agglomerated into nanowires, nanorods, nanoleafs, and coconut shell-like morphologies due to the stirring effect and the increase of DMF concentration. The crystallite sizes and surface areas of the CZC catalysts are consistent with the distinct morphologies observed in the SEM micrographs.
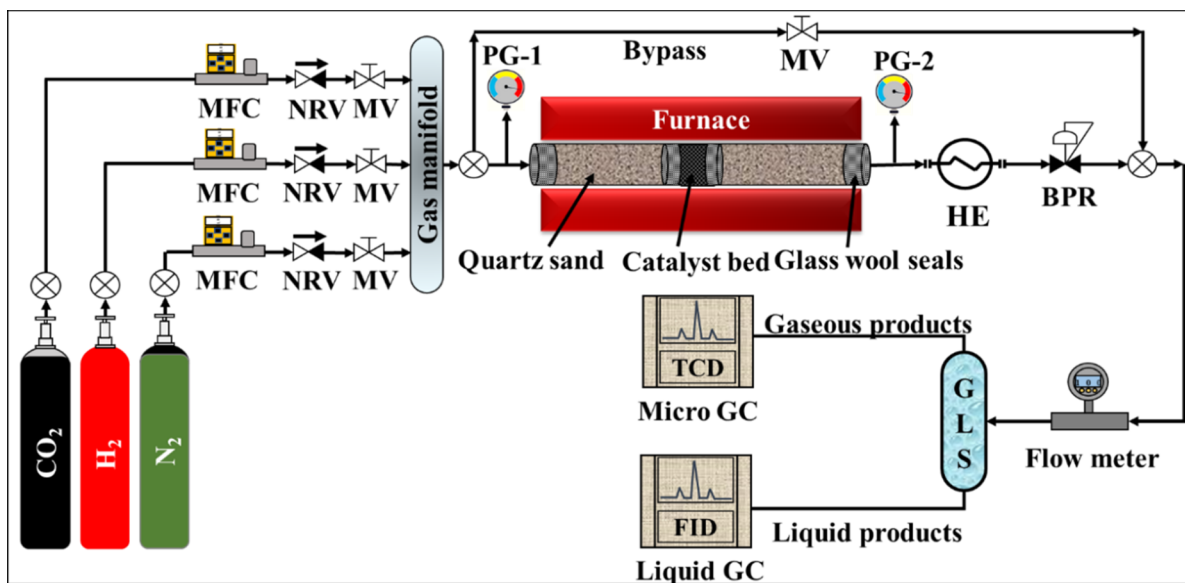
Fig. 1 Schematic of experimental setup used in present study. (MFC: mass flow controller, NRV: non-return valve, MV: manual valve, HE: heat exchanger, BPR: back pressure regulator, GLS: gas–liquid separator, GC: gas chromatography.)

3.4. X-ray photoelectron spectroscopy (XPS) analysis

The deconvolution of the CZC catalysts' Cu 2p, Zn 2p, Ce 3d, and O 1s spectra are displayed in Fig. 5(a)–(d). The deconvolution of the Cu 2p core level spectra revealed the presence of the Cu^+ and Cu^{2+} species, with binding energies of 932.2 eV and 933.8 eV.[21] The spin-orbital ratio of Cu $2p_{3/2}$ to Cu $2p_{1/2}$ was kept at 2 : 1 with a separation of 19.8 eV. The Cu^{2+} state of CuO is confirmed by a satellite peak at 942.5 eV.[22] The CZC catalysts revealed the presence of both Cu^+ and Cu^{2+} species. From the analysis, it is observed that the CZC-1 catalyst displayed a higher ratio of Cu^+/Cu^{2+} compared to the other two catalysts. The

presence of surface Cu^+ species is of significant importance as it plays a pivotal role in facilitating CO_2 adsorption and H_2 dissociation, essential steps in the CO_2 hydrogenation catalytic process. The Zn 2p core level spectrum was deconvoluted into two peaks, corresponding to the Zn^0 and Zn^{2+} states, with binding energies of 1021.6 eV and 1022.6 eV.[23] The separation of Zn $2p_{3/2}$ and Zn $2p_{1/2}$ was found to be 23 eV while maintaining the doublet ratio as 2 : 1. The Ce 3d core level spectrum of Ce $3d_{5/2}$ and Ce $3d_{3/2}$ were deconvoluted into two doublets which corresponds to Ce^{3+} (882.0 eV and 883.8 eV; 900.6 eV and 902.4 eV) and Ce^{4+} (888.7 eV and 897.9 eV; 907.3 eV and 916.3 eV) state of CeO_2.[24] For Ce^{3+} and Ce^{4+} peaks, 3 : 2 spin-orbital ratio of Ce
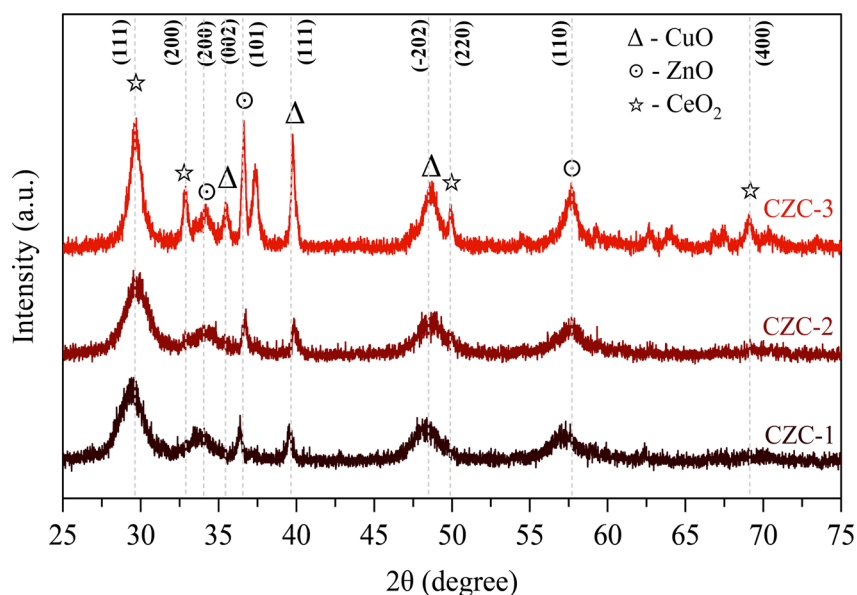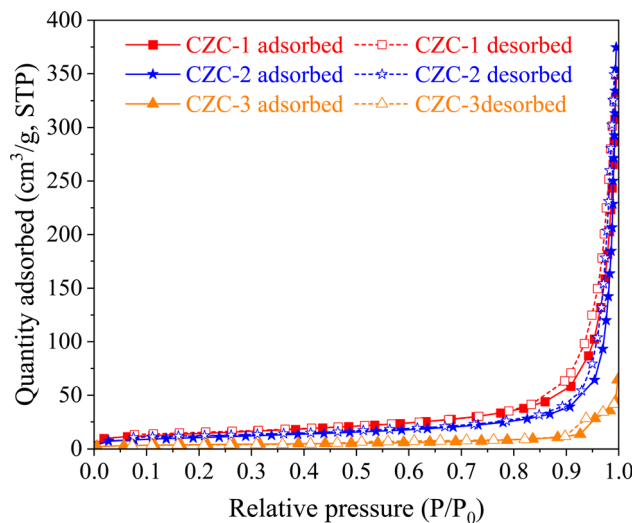

Fig. 2 XRD patterns of CZC catalysts.

Table 1 Physico-chemical properties of CZC catalysts

Catalysts	Crystallite size (nm)	S_{BET} (m^2 g^{-1})	O_V (%)	Ce^{3+}/Ce^{4+}	Cu^+/Cu^{2+}	$CuO_{dispersion}$ (%)	H_2 consumption (μmol g_{cat}^{-1})
CZC-1	9.1	51.1	29.3	0.80	0.93	48.1	2129
CZC-2	12.1	36.6	27.6	0.76	0.79	27.7	2034
CZC-3	17.8	14.1	27.4	0.73	0.61	23.8	1960

Fig. 3 N$_2$ adsorption–desorption isotherms of CZC catalysts.

3d$_{5/2}$ to Ce 3d$_{3/2}$ was followed with a separation of 18.6 eV. The formation of oxygen vacancies is consistent with the concentration of Ce^{3+} on the catalyst surface. Table 1 provides the Ce^{3+}/Ce^{4+} values of three CZC catalysts. The data indicates that the Ce^{3+}/Ce^{4+} value for the CZC-1 catalyst is highest, indicating more oxygen vacancies on its surface. Based on the lattice oxygen (O$_L$), vacant oxygen (O$_V$), and hydroxyl oxygen (O$_H$) with the binding energies of 529.3 eV, 531.5 eV, and 533 eV, the O 1s core level spectrum was deconvoluted. The concentration Ov could be assumed as O$_V$/(O$_L$ + O$_V$ + O$_H$). As shown in Fig. 5(d), the concentration of Ov orders is in the following order: CZC-1 > CZC-2 > CZC-3. The density of O$_V$ in the O 1s spectra outcomes of three CZC catalysts is consistent with the corresponding Ce 3d spectra analysis.

3.5. Temperature-programmed reduction analysis

Fig. 6 shows the H$_2$-TPR profiles of the CZC catalysts. The Fityk open-source software was used to deconvolute the broad reduction peak between 180 °C and 240 °C in H$_2$-TPR profiles into three Gaussian peaks. The peak between 180 °C and 200 °C ascribed to the reduction of strong metal–support interactions of dispersed CuO species. The reduction peak of weak metal–support interactions of dispersed CuO species occurs between 200 °C and 220 °C. The peak between 230 °C and 250 °C corresponds to the bulk CuO reduction.[25,26] The reduction of ZnO and CeO$_2$ is attributed to the peaks between 250 °C and 800 °C. Eqn (2) was used to calculate the surface CuO dispersion (CuO$_{dispersion}$) based on the CuO reduction peak areas. The CuO$_{dispersion}$ and H$_2$ consumption data are given in Table 1. The analysis revealed that the CuO$_{dispersion}$ of the catalytic surface
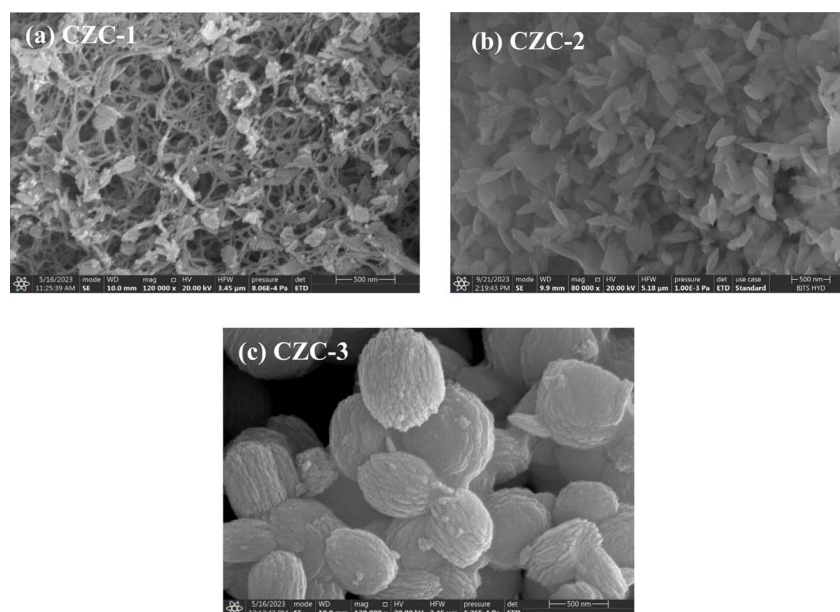

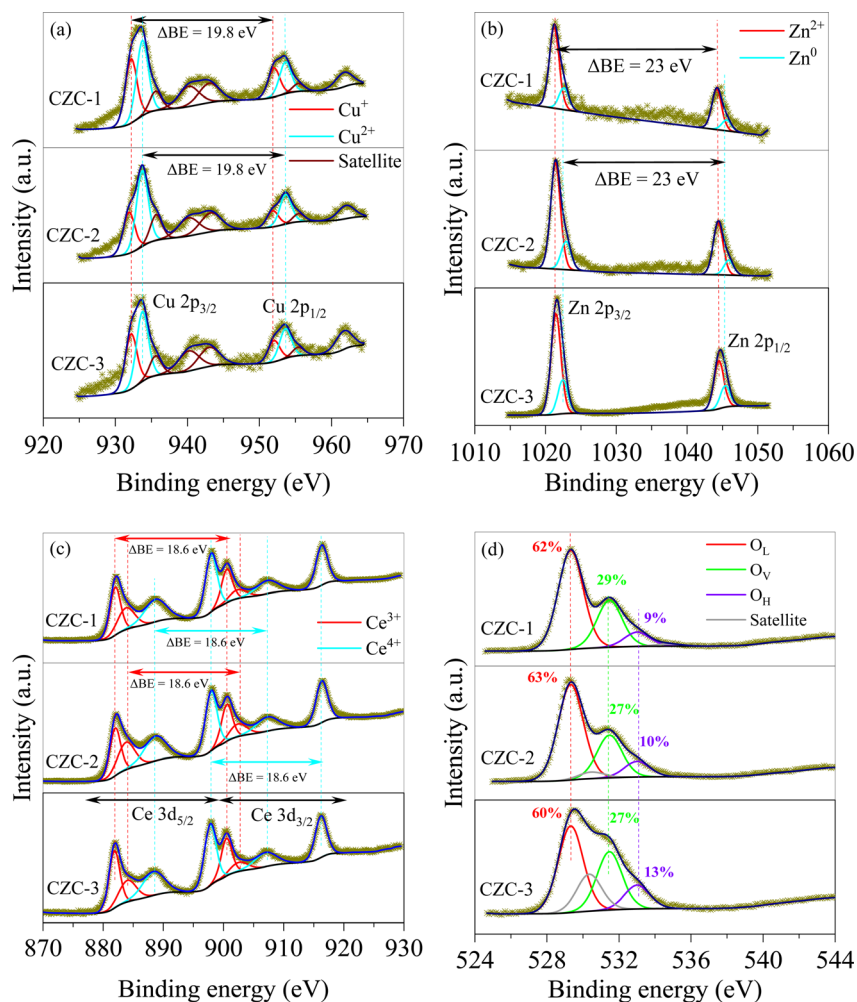**Fig. 4** SEM micrographs of CZC catalysts.

Fig. 5 XPS spectra of CZC catalysts (a) Cu 2p, (b) Zn 2p, (c) Ce 3d, and (d) O 1s.

decreases as the catalyst is synthesized with stirring and an increase in DMF concentration.

$$CuO_{dispersion} \ (\%) = \frac{(A_{area} + B_{area})}{(A_{area} + B_{area} + C_{area})} \times 100 \qquad (2)$$

3.6. FTIR spectroscopy analysis

FTIR analysis was conducted for the liquid products obtained from the CO_2 hydrogenation to methanol experiments, employing three distinct CZC catalysts. The spectra of the liquid products were compared with the IR spectra of pure methanol and water recorded under similar conditions. Fig. 7 presents the FTIR spectra of pure methanol, water, and liquid product samples of CZC materials. Peaks observed at 3330 cm^{-1}, 2944 cm^{-1}, 2833 cm^{-1}, 1413 cm^{-1}, 1114 cm^{-1}, and 1021 cm^{-1} correspond to pronounced absorption bands associated with various vibrational modes in pure methanol sample.[27] Specifically, these include O–H stretching, C–H asymmetric stretching, C–H symmetric stretching, C–H out-plane bending (wagging and twisting), and C–H in-plane bending (scissoring and

rocking), as well as C–O stretching vibrations. Additionally, peaks at 3330 cm^{-1} and 1641 cm^{-1} are attributed to the O–H stretching and H–O–H bending vibrations of water samples.[28] The FTIR spectra of the three CZC catalyst liquid product samples revealed distinct peaks corresponding to both methanol and water, indicating that the sample is a mixture of methanol and water. Further, the quantification of methanol in the liquid product samples was validated through gas chromatography analysis employing a flame ionization detector (FID).

3.7. Performance of CZA catalysts towards MeOH selectivity from CO_2 and H_2

The catalytic activity of the catalysts was carried out at 225 °C, 30 bar pressure, and an H_2/CO_2 mole ratio of 3. The CO_2 conversion (X_{CO2}), methanol selectivity (S_{MeOH}), CO selectivity (S_{CO}), and methanol yield (Y_{MeOH}) were determined using the following equations (eqn (3)–(6)). The heat and mass transport limitations of the present catalytic system were verified by using Anderson criterion and Weisz–Prater criterion.[29,30] The analysis showed that the present investigation is free from heat and
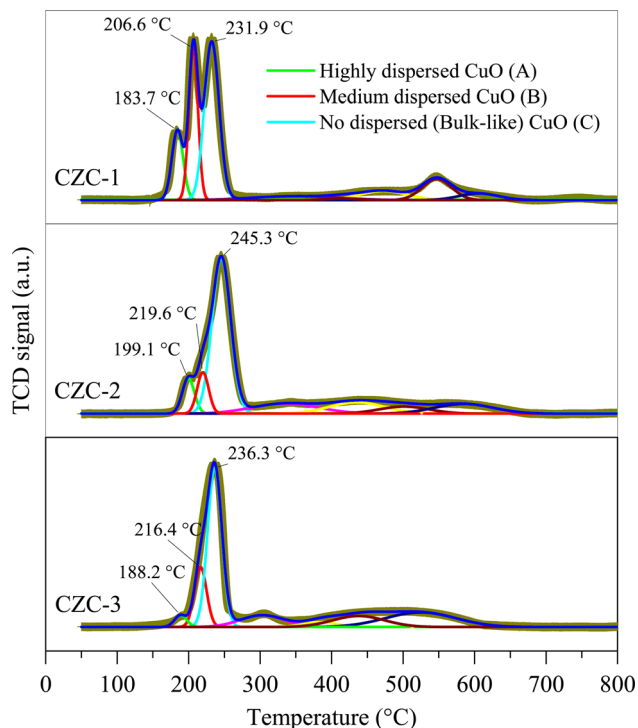
Fig. 6 H₂-TPR profiles of CZC catalysts.

Fig. 8 Catalytic performance of CZC catalysts (experimental conditions: $T = 225\ °C$, $P = 30$ bar, WHSV = 6000 cm³ $(g_{cat}\ h)^{-1}$, and H_2/CO_2 mole ratio = 3).

$$X_{CO_2}\ (\%) = \left(1 - \frac{F_{CO_2,out}}{F_{CO_2,in}}\right) \times 100 \qquad (3)$$

$$S_{MeOH}\ (\%) = \left(\frac{(F_{MeOH,out})}{(F_{MeOH,out}) + (F_{CO,out})}\right) \times 100 \qquad (4)$$

$$S_{CO}\ (\%) = \left(\frac{(F_{CO,out})}{(F_{MeOH,out}) + (F_{CO,out})}\right) \times 100 \qquad (5)$$

$$Y_{MeOH}\ (\%) = (X_{CO_2})(S_{MeOH}) \times 100 \qquad (6)$$

where 'F_i' is molar flow rate of component i.

mass transfer limitations. The outcomes of the investigation were examined in terms of CO_2 conversion, selectivity of MeOH, and CO, and yield of MeOH as shown in Fig. 8. With 13.6% CO_2 conversion and 74% methanol selectivity, the nanowire-like catalyst (*i.e.*, CZC-1) showed superior activity compared to the other two catalysts. The increased MeOH yield and CO_2 conversion with the CZC-1 catalyst might be attributed due to improved physico-chemical properties such as strong metal–support interactions, $CuO_{dispersion}$, BET surface area, and oxygen vacancies of the catalyst.
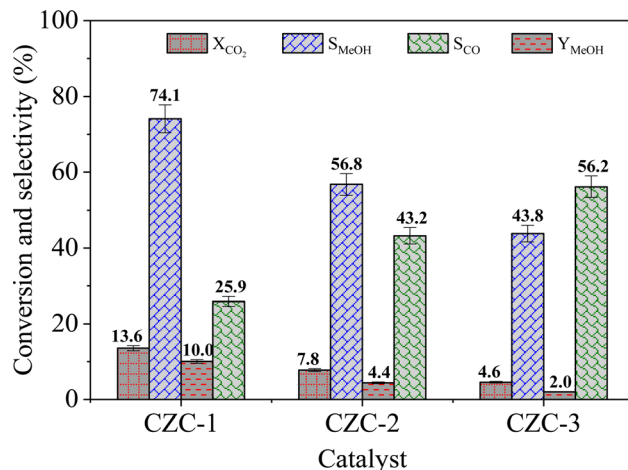
Among the nanowires, nanoleafs, and coconut shells morphologies, the nanowire morphology (*i.e.*, for CZC-1) demonstrated a notably higher surface area-to-volume ratio. This characteristic is pivotal as it facilitates contact between the
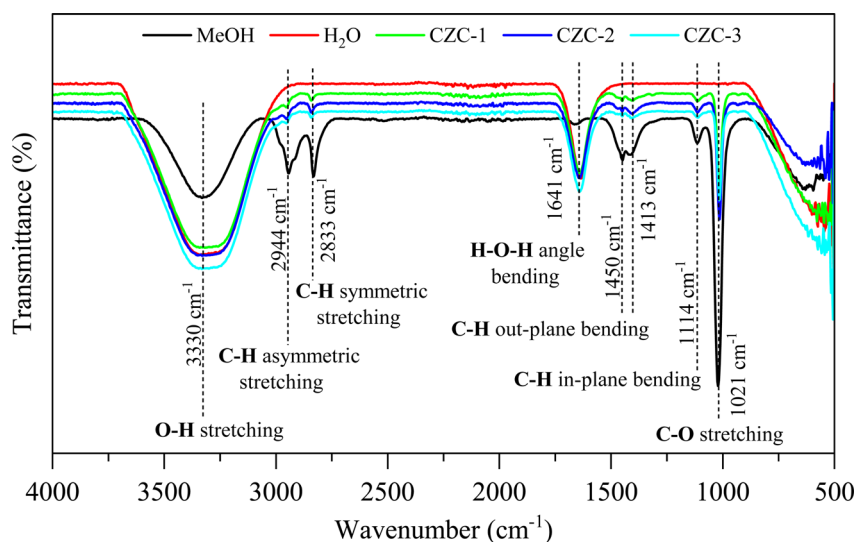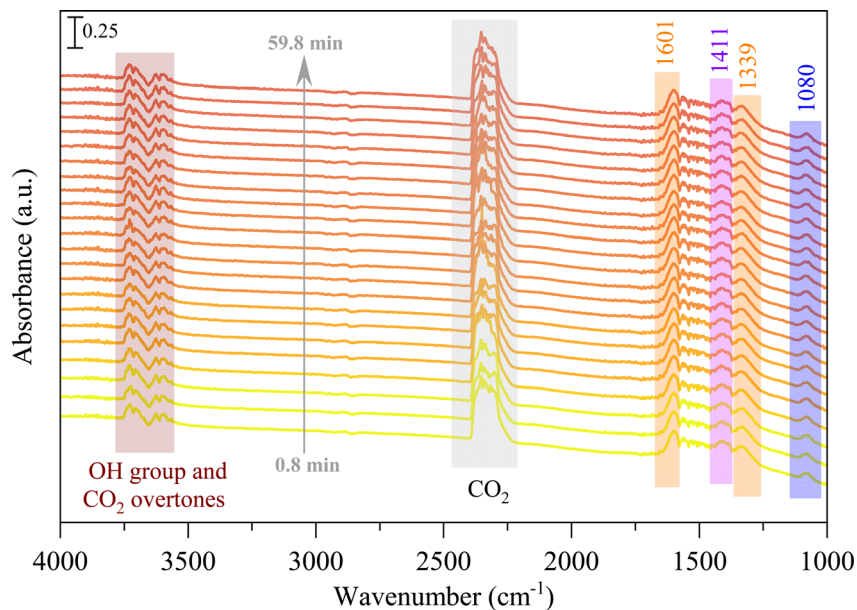

Fig. 7 FTIR spectra of liquid products.

Fig. 9 *In situ* DRIFTS spectra of CZC-1 catalyst under atmospheric pressure and 225 °C.

active sites of the CZC-1 catalyst and the reactants (*i.e.*, CO_2 and H_2), thereby enhancing the conversion of CO_2 to methanol. The findings derived from the BET surface area and XRD analyses of the CZC catalysts directly corresponded to their respective morphologies, as summarized in Table 1. XPS analysis of the CZC catalysts revealed the presence of Cu^+, Cu^{2+}, Ce^{3+}, Ce^{4+}, and oxygen vacancies. Notably, CZC-1 exhibited a higher concentration of oxygen vacancies, along with an augmented ratio of Cu^+/Cu^{2+} and Cu^{3+}/Cu^{4+}. The surface oxygen vacancies and Ce^{3+} species are crucial in enhancing CO_2 adsorption, while Cu^+ species facilitate H_2 dissociation. Based on the H_2-TPR analysis

of CZC catalysts, prominent CuO reduction peaks are observed between 180 °C and 240 °C. The low-temperature CuO reduction behavior of CZC-1 suggests superior dispersion of fine CuO species on the catalyst surface. The increased dispersion facilitates effective contact between reactants and a higher proportion of catalyst sites (CuO and CeO_2). Consequently, the improved CuO dispersion facilitates enhanced CO_2 adsorption and H_2 dissociation, pivotal steps in the catalytic process, thus augmenting the conversion of CO_2 to methanol.

This holistic analysis confirms that the CZC-1 catalyst exhibits enhanced CuO surface dispersion, nanowire-like
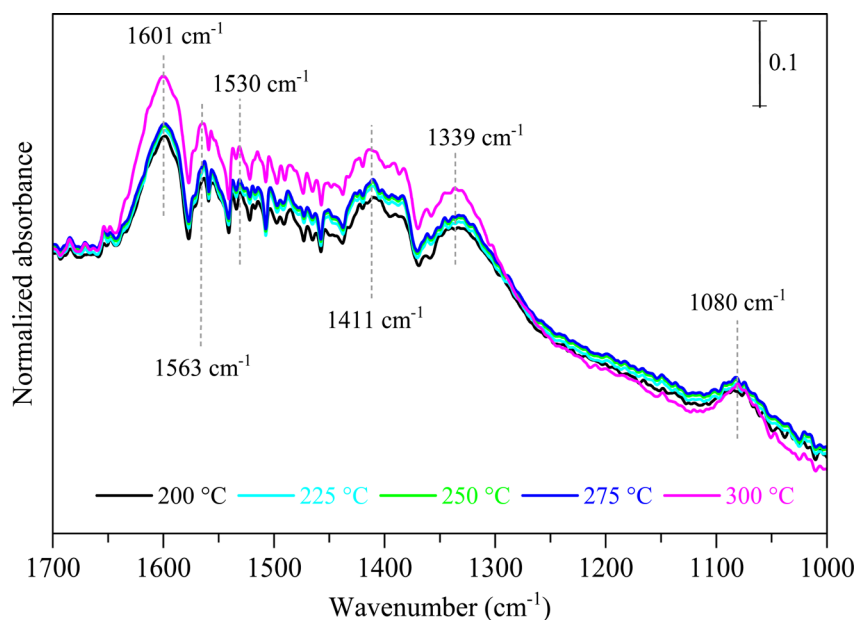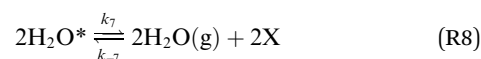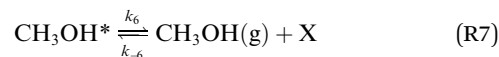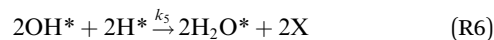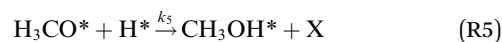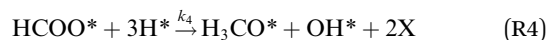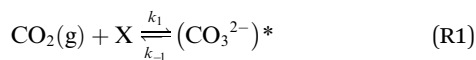

Fig. 10 Influence of temperature on *in situ* DRIFTS spectra during CO_2 hydrogenation over CZC-1 catalyst under 1 bar pressure.

morphology, and improved oxygen vacancies. The presence of Cu^+ state enables the dissociation of hydrogen molecules, which is crucial for subsequent reactions. Furthermore, the improved oxygen vacancy induced by the Cu^+ and Ce^{3+} constituents within the composite catalyst enhanced the CO_2 adsorption onto the catalyst surface, consequently improving CO_2 conversion rates. Moreover, the adsorbed CO_2 and dissociated hydrogen react through formate and methoxy intermediates, facilitating the enhancement of methanol yield.

3.8. *In situ* FTIR analysis

The *in situ* DRIFTS analysis was performed to identify the probable mechanism/pathway of MeOH formation from CO_2 hydrogenation reaction. Fig. 9 displays the *in situ* DRIFTS spectra of the CZC-1 catalyst at 225 °C and 1 bar pressure. The peaks at 3700 cm^{-1} and 3600 cm^{-1} are ascribed to CO_2 overtones, while the neighboring peaks at 3730 cm^{-1} and 3630 cm^{-1} are associated to the hydroxyl groups on the catalyst surface.[31] The prominent peak at 1411 cm^{-1} can be assigned to the carbonate species (CO_3^{2-}).[32–34] The strong IR bands at 1080 cm^{-1}, 1339 cm^{-1}, and 1601 cm^{-1} attributed to the C–O stretching vibrations of methoxy (CH_3O^*), and symmetric and asymmetric O–C–O stretching vibrations of formate ($CHOO^*$).[35–37] According to DRIFTS data at 225 °C (Fig. 9), the initial phase involves CO_2 adsorption onto the oxygen vacancies of the catalyst, leading to the formation of carbonate species (observed at 1411 cm^{-1}). Subsequently, through a series of reactions, carbonate species undergo hydrogenation *via* dissociative hydrogen, resulting in the generation of $CHOO^*$ (noted at 1339 cm^{-1} and 1601 cm^{-1}) and CH_3O^* (observed at 1080 cm^{-1}).

To investigate the impact of temperature on the formation and hydrogenation of intermediate species during the CO_2 hydrogenation reaction, the DRIFTS experiments were conducted at five distinct temperatures: 200 °C, 225 °C, 250 °C, 275 °C, and 300 °C, as illustrated in Fig. 10. Upon analysis, a noticeable pattern occurs as the temperature increases from 200 °C to 300 °C. The result indicates a significant increase in carbonate species, as evidenced by peaks at 1530 cm^{-1} and 1411 cm^{-1}, suggesting that the higher temperature promoted the increase of CO_2 adsorption on the vacant oxygen sites of the catalyst.[38] This rise in carbonate species quantity appears to accelerate the hydrogenation process, leading to the formation of formate species, as indicated by peaks at 1339 cm^{-1}, 1563 cm^{-1}, and 1601 cm^{-1}.[39] Thus, based on the DRIFTS analysis, it can be concluded that the CO_2 hydrogenation to methanol reaction follows the carbonate–formate–methoxy reaction pathway in the presence of CZC-1 catalyst. Based on the identified intermediates from the *in situ* DRIFTS analysis, the following reaction scheme (*i.e.*, (R1)–(R8)) may be proposed for the CO_2 hydrogenation.

$$CO_2(g) + X \underset{k_{-1}}{\overset{k_1}{\rightleftharpoons}} (CO_3^{2-})^* \tag{R1}$$

$$4H_2(g) + 8X \underset{k_{-2}}{\overset{k_2}{\rightleftharpoons}} 8H^* \tag{R2}$$

$$(CO_3^{2-})^* + 2H^* \overset{k_3}{\rightarrow} HCOO^* + OH^* + X \tag{R3}$$

$$HCOO^* + 3H^* \overset{k_4}{\rightarrow} H_3CO^* + OH^* + 2X \tag{R4}$$

$$H_3CO^* + H^* \overset{k_5}{\rightarrow} CH_3OH^* + X \tag{R5}$$

$$2OH^* + 2H^* \overset{k_5}{\rightarrow} 2H_2O^* + 2X \tag{R6}$$

$$CH_3OH^* \underset{k_{-6}}{\overset{k_6}{\rightleftharpoons}} CH_3OH(g) + X \tag{R7}$$

$$2H_2O^* \underset{k_{-7}}{\overset{k_7}{\rightleftharpoons}} 2H_2O(g) + 2X \tag{R8}$$

where, X is the catalyst vacant site (or oxygen vacant site), and a superscript * indicates the corresponding adsorbed species.

4. Conclusion

The present study investigates the impact of catalyst surface morphology on CZC catalyst for MeOH synthesis *via* CO_2 hydrogenation reaction. The morphologically modified composite $CuO–ZnO–CeO_2$ catalysts were synthesized employing a single-step hydrothermal technique. A nanowire-like morphology of catalysts was confirmed from the SEM analysis. The BET surface area of the catalysts was in the range of 14–51 m^2 g^{-1}. The existence of more oxygen vacancies, the Cu^+ state of CuO, and the Ce^{3+} state of CeO_2 in CZC catalysts was confirmed by the XPS analysis. According to the H_2-TPR study, the CZC-1 catalyst demonstrates 48.1% $CuO_{dispersion}$. Among the three catalysts, the CZC-1 catalyst showed better performance with a 13.6% CO_2 conversion and 74.1% methanol selectivity at 225 °C, 30 bar pressure, and for a space velocity of 6000 cm^3 g_{cat}^{-1} h^{-1}. Moreover, the *in situ* DRIFTS analysis conclusively confirmed the carbonate–formate–methoxy reaction pathway as the reaction mechanism for MeOH formation through CO_2 hydrogenation in the presence of the CZC-1 catalyst.

Author contributions

Suresh Kanuri: conceptualization, investigation, data generation, writing-original draft; Satyapaul A. Singh: conceptualization, result validation, supervision, methodology; Appala Naidu Uttaravalli: data verification, writing-editing; Sounak Roy: result validation, writing-editing; Srikanta Dinda: data verification, supervision, writing-editing, administration.

Conflicts of interest

The authors declare that they have no known competing financial interests or personal relationships that could have appeared to influence the work reported in this manuscript.

Acknowledgements

References

1 S. Poto, D. Vico, V. Berkel, F. Gallucci and M. F. Neira, *Chem. Eng. J.*, 2022, **435**, 134946.

2 H. R. Darji, H. B. Kale, F. F. Shaikh and M. B. Gawande, *Coord. Chem. Rev.*, 2023, **497**, 215409.

3 S. Kanuri, J. D. Vinodkumar, S. P. Datta, C. Chakraborty, S. Roy, S. A. Singh and S. Dinda, *Korean J. Chem. Eng.*, 2023, **40**, 810–823.

4 J. Zhong, X. Yang, Z. Wu, B. Liang, Y. Huang and T. Zhang, *Chem. Soc. Rev.*, 2020, **49**, 1385–1413.

5 S. Kanuri, S. Roy, C. Chakraborty, S. P. Datta, S. A. Singh and S. Dinda, *Int. J. Energy Res.*, 2022, **46**, 5503–5522.

6 H. Mahajan and S. Cho, *RSC Adv.*, 2022, **12**, 9112–9120.

7 C. Zhong, X. Guo, D. Mao, S. Wang, G. Wu and G. Lu, *RSC Adv.*, 2015, **5**, 52958–52965.

8 W. L. Ng, P. Sripada, S. Biswas and S. Bhattacharya, *Appl. Catal., A*, 2022, **646**, 118885.

9 B. Ouyang, W. Tan and B. Liu, *Catal. Commun.*, 2017, **95**, 36–39.

10 Q. Tan, Z. Shi and D. Wu, *Ind. Eng. Chem. Res.*, 2018, **57**, 10148–10158.

11 J. Zhu, D. Ciolca, L. Liu, A. Parastaev, N. Kosinov and E. J. M. Hensen, *ACS Catal.*, 2021, **11**, 4880–4892.

12 S. K. Sharma, B. Paul, R. S. Pal, P. Bhanja, A. Banerjee, C. Samanta and R. Bal, *ACS Appl. Mater. Interfaces*, 2021, **13**, 28201–28213.

13 R. Singh, K. Tripathi and K. K. Pant, *Fuel*, 2021, **303**, 121289.

14 S. F. Zaman, O. A. Ojelade, H. Alhumade, J. Mazumder, H. Omar and P. Casta, *Fuel*, 2023, **343**, 127927.

15 L. Kong, Y. Shi, J. Wang, P. Lv, G. Yu and W. Su, *Catal. Lett.*, 2023, **153**, 477–492.

16 Y. Yan, R. Jien, Z. Ma, F. Donat, S. Xi, S. Saqline, Q. Fan, Y. Du, A. Borgna, Q. He, C. R. Müller, W. Chen, A. A. Lapkin and W. Liu, *Appl. Catal., B*, 2022, **306**, 121098.

17 M. A. Rossi, L. H. Vieira, L. F. Rasteiro, M. A. Fraga, J. M. Assaf and E. M. Assaf, *React. Chem. Eng.*, 2022, **7**, 1589–1602.

18 R. Khobragade, M. Roskaric, G. Zerjav, M. Kosicek, J. Zavasnik, N. Van De Velde, I. Jerman, N. N. Tusar and A. Pintar, *Appl. Catal., A*, 2021, **627**, 118394.

19 F. Xie, S. Xu, L. Deng and H. Xie, *Int. J. Energy Res.*, 2020, **45**, 26938–26952.

20 F. Jiang, S. Wang, B. Liu, J. Liu, L. Wang, Y. Xiao, Y. Xu and X. Liu, *ACS Catal.*, 2020, **10**, 11493–11509.

21 C. Si, H. Ban, K. Chen, X. Wang, R. Cao, Q. Yi, Z. Qin, Z. Li, W. Cai and C. Li, *Appl. Catal., A*, 2020, **594**, 117466.

22 A. Bhardwaj, A. S. Ahluwalia, K. K. Pant and S. Upadhyayula, *Sep. Purif. Technol.*, 2023, **324**, 124576.

23 O. A. Ojelade, S. F. Zaman, M. A. Daous, A. A. Al-zahrani, A. S. Malik, H. Driss, G. Shterk and J. Gascon, *Appl. Catal., A*, 2019, **584**, 117185.

24 A. S. Malik, S. F. Zaman, A. A. Al-zahrani, M. A. Daous, H. Driss and L. A. Petrov, *Appl. Catal., A*, 2018, **560**, 42–53.

25 P. Ren, W. Tu, C. Wang, S. Cheng, W. Liu, Z. Zhang, Y. Tian and Y. Han, *Appl. Catal., B*, 2022, **305**, 121016.

26 Z. Shi, Q. Tan and D. Wu, *Appl. Catal., A*, 2019, **581**, 58–66.

27 M. I. Tejedor-Tejedor, L. Paredes and M. A. Anderson, *Chem. Mater.*, 1998, **10**, 3410–3421.

28 L. Mercantili, F. Davis and S. P. J. Higson, *J. Surfactants Deterg.*, 2014, **17**, 133–141.

29 D. E. Mears, *J. Catal.*, 1971, **20**, 127–131.

30 V. Prasad, A. M. Karim, A. Arya and D. G. Vlachos, *Ind. Eng. Chem. Res.*, 2009, **48**, 5255–5265.

31 F. Hu, C. Jin, R. Wu, C. Li, G. Song, T. Z. H. Gani, K. H. Lim, W. Guo, T. Wang, S. Ding, R. Ye, Z. H. Lu, G. Feng, R. Zhang and S. Kawi, *Chem. Eng. J.*, 2023, **461**, 142108.

32 Y. Wei, F. Liu, J. Ma, C. Yang, X. Wang and J. Cao, *Mol. Catal.*, 2022, **525**, 112354.

33 K. Lee, U. Anjum, T. P. Araújo, C. Mondelli, Q. He, S. Furukawa, J. Pérez-Ramírez, S. M. Kozlov and N. Yan, *Appl. Catal., B*, 2022, **304**, 120994.

34 J. Sun, F. Liu, U. Salahuddin, M. Wu, C. Zhu, X. Lu, B. Zhang, B. Zhao, Z. Xie, Y. Ding, D. Li, C. Y. Nam, F. Y. Zhang and P. X. Gao, *Chem. Eng. J.*, 2023, **455**, 140559.

35 S. Kanuri, S. Dinda, S. A. Singh, S. Roy, C. Chakraborty and S. P. Datta, *Mater. Today Chem.*, 2024, **36**, 101959.

36 S. Kanuri, S. A. Singh and S. Dinda, *Chem. Eng. Sci.*, 2024, **286**, 119661.

37 J. Chen, B. Wu, Y. Shao, H. Guo and H. Chen, *AIChE J.*, 2023, 1–14.

38 Y. H. Wang, W. G. Gao, H. Wang, Y. E. Zheng, W. Na and K. Z. Li, *RSC Adv.*, 2017, **7**, 8709–8717.

39 Y. Wang, Y. Wei, Y. Li, X. Chen, J. Caro and A. Huang, *ChemCatChem*, 2023, **15**, 1–6.